scientific reports

Check for updates

OPEN

Differentiating *MYCN*-amplified *RB1* wild-type retinoblastoma from biallelic *RB1* mutant retinoblastoma using MR-based radiomics: a retrospective multicenter case–control study

Christiaan M. de Bloeme [1,2,3]✉, Robin W. Jansen[1,2,3], Liesbeth Cardoen[1,4], Sophia Göricke[1,5], Sabien van Elst[1,2,3], Jaime Lyn Jessen[6], Aparna Ramasubramanian[7], Alison H. Skalet[8,9], Audra K. Miller[8], Philippe Maeder[1,10], Ogul E. Uner[8,11], G. Baker Hubbard[11], Hans Grossniklaus[11], H. Culver Boldt[12], Kim E. Nichols[13], Rachel C. Brennan[13,14], Saugata Sen[15], Mériam Koob[1,10], Selma Sirin[1,16], Hervé J. Brisse[1,4], Paolo Galluzzi[1,17], Charlotte J. Dommering[2,18], Matthijs Cysouw[2,3], Ronald Boellaard[2,3], Josephine C. Dorsman[2,19], Annette C. Moll[2,20], Marcus C. de Jong[1,2,3], Pim de Graaf[1,2,3] & European Retinoblastoma Imaging Collaboration

***MYCN*-amplified *RB1* wild-type (*MYCN*^{amp}*RB1*$^{+/+}$) retinoblastoma is a rare and aggressive subtype, often resistant to standard therapies. Identifying unique MRI features is crucial for diagnosing this subtype, as biopsy is not recommended. This study aimed to differentiate *MYCN*^{amp}*RB1*$^{+/+}$ from the most prevalent *RB1*$^{-/-}$ retinoblastoma using pretreatment MRI and radiomics. Ninety-eight unilateral retinoblastoma patients (19 *MYCN* cases and 79 matched controls) were included. Tumors on T2-weighted MR images were manually delineated and validated by experienced radiologists. Radiomics analysis extracted 120 features per tumor. Several combinations of feature selection methods, oversampling techniques and machine learning (ML) classifiers were evaluated in a repeated fivefold cross-validation machine learning pipeline to yield the best-performing prediction model for *MYCN*. The best model used univariate feature selection, data oversampling (duplicating *MYCN* cases), and logistic regression classifier, achieving a mean AUC of 0.78 (SD 0.12). SHAP analysis highlighted lower *sphericity*, higher *flatness*, and greater *gray-level heterogeneity* as predictive for *MYCN*^{amp}*RB1*$^{+/+}$ status, yielding an AUC of 0.81 (SD 0.11). This study shows the potential of MRI-based radiomics to distinguish *MYCN*^{amp}*RB1*$^{+/+}$ and *RB1*$^{-/-}$ retinoblastoma subtypes.**

Keywords Retinoblastoma, MRI; radiomics , *MYCN*-amplification

Abbreviations

RB1$^{-/-}$	Pathogenic variants in the *RB1* gene
MYCN^{amp}*RB1*$^{+/+}$	*MYCN*-amplified *RB1* wild-type
MRI	Magnetic resonance imaging
STARD	Standards for Reporting Diagnostic accuracy studies
PCA	Principal component analysis
RFE-LR	Recursive feature elimination approach using a logistic regression in nested cross-validation
RFE-RF	Recursive feature elimination approach using random forest in nested cross-validation
Univariate	Univariate selection method based on ANOVA testing that retained the top 10 percentile features
AUC	Area under the curve
SD	Standard deviation

[1]European Retinoblastoma Imaging Collaboration (ERIC), Amsterdam, The Netherlands. [2]Cancer Center Amsterdam, Imaging and Biomarkers, Amsterdam, The Netherlands. [3]Department of Radiology and Nuclear Medicine, UMC location Vrije Universiteit Amsterdam, Amsterdam 1007 MB, The Netherlands. [4]Imaging department Institut Curie, France and Paris-Siences-et-Lettres University, Paris, France. [5]Department of Diagnostic and Interventional Radiology and Neuroradiology, University Hospital Essen, Essen, Germany. [6]Impact Genetics - Dynacare, Ontario, Canada. [7]Department of Ophthalmology, Children's Wisconsin, Wisconsin, United States. [8]Casey Eye Institute Oregon Health & Science University , Portland, United States. [9]Knight Cancer Institute Oregon Health & Science University, Portland, United States. [10]Department of Radiology Centre Hospitalier Universitaire Vaudois (CHUV) , University of Lausanne , Lausanne, Switzerland. [11]Emory Eye Center Ocular Oncology Service, Atlanta, United States. [12]Department of Ophthalmology, University of Iowa Hospitals & Clinics, Iowa, United States. [13]Department of Oncology, St. Jude Children's Research Hospital, Memphis, United States. [14]Department of Pediatric Hematology/Oncology, Logan Health, Kalispell (Montana), United States. [15]Department of Radiology and Imaging Sciences, Tata Medical Center, Kolkata, India. [16]Department of Diagnostic Imaging, University Children's Hospital Zurich University of Zurich, Zurich, Switzerland. [17]Department of Neuroimaging unit, Siena University Hospital, Siena, Italy. [18]Department of Human Genetics, Amsterdam UMC location Vrije Universiteit, Amsterdam, The Netherlands. [19]Department of Oncogenetics, UMC location Vrije Universiteit, Amsterdam, The Netherlands. [20]Department of Ophthalmology, UMC location Vrije Universiteit Amsterdam, Amsterdam, The Netherlands. ✉email: c.debloeme@amsterdamumc.nl

Retinoblastoma is the most prevalent malignant ocular neoplasm in pediatric patients with an incidence of 1:17,000 live births and is typically diagnosed before the age of five[1]. The initiation of tumorigenesis primarily involves biallelic inactivation of the *RB1* tumor suppressor gene, resulting in $RB1^{-/-}$ retinoblastoma. It has been established that distinct molecular subtypes of retinoblastoma exist, offering potential avenues for individualized therapeutic interventions[2–8].

In 2013 a subtype of retinoblastoma was identified, characterized by a significant amplification of *MYCN* in the tumor without detectable pathogenic variants in the *RB1* alleles($MYCN^{amp}RB1^{+/+}$). In this subtype, *MYCN* amplification was identified as the key driver in initiating retinal tumors, observed in approximately 1–2% of retinoblastoma cases[9–11]. Although *MYCN* amplifications can also be found in $RB1^{-/-}$ tumors, *RB1* wild-type ($RB1^{+/+}$) tumors with *MYCN* amplification ($MYCN^{amp}RB1^{+/+}$) show a clear inclination and exhibiting unique clinical characteristics[12,13]. A previous study revealed that this $MYCN^{amp}RB1^{+/+}$ retinoblastoma manifests as unilateral large tumors at an early age, displaying distinctive histopathological features characterized by poorly differentiated neuroblastic cells and limited rosette formations[9]. Moreover, this subtype demonstrated relative resistance to conventional therapeutic interventions[14]. The diagnosis of retinoblastoma in children under 12 months of age frequently indicates an inherited condition with increased risk of bilateral disease and subsequent significant loss of vision, which enhances efforts to pursue eye-saving therapeutic approaches. However, caution must be exercised when considering eye salvage in this aggressive subtype of retinoblastoma. Hence, early identification of patients with $MYCN^{amp}RB1^{+/+}$ retinoblastoma holds significant clinical importance, as it may facilitate the implementation of a tailored treatment strategy.

Clinical detection of genetic characteristics in retinoblastoma is challenging due to limited availability of histopathologic material for molecular testing. Tumor biopsy is contraindicated due to the risks of local tumor seeding and metastasis. Additionally, there is a decreasing availability of enucleated specimens as eye-saving treatment options are more commonly employed, even in advanced-stage cases[15,16]. Therefore, the development of methods to stratify tumor subtypes in-vivo and implement targeted therapies is crucial. A promising technique involves obtaining cell-free tumor DNA from the aqueous humor[17], however this approach requires an invasive procedure and is not yet in widespread use. Another emerging, and non-invasive technique, is magnetic resonance imaging (MRI), which is widely utilized in retinoblastoma for diagnostic support, disease staging, and screening for intracranial trilateral disease[18–20]. Qualitative analysis of MR images showed $MYCN^{amp}RB1^{+/+}$ retinoblastoma can be differentiated from the subtype $RB^{-/-}$ retinoblastoma in a case–control study with very young unilaterally affected retinoblastoma patients[21]. The *MYCN*-amplified *RB1* wild-type more frequently exhibits specific features such as a peripheral location, peritumoral hemorrhage, subretinal hemorrhage with fluid–fluid level and retinal folding with vitreous enclosure[21]. In addition to qualitative analysis of MR images, these same images can be utilized for quantitative data extraction through radiomics—a potential tool in oncology research to enhance personalized medicine[22]. Some exploratory radiomics studies have been conducted in the field of retinoblastoma[23,24]. Notably, Li et al.'s 2022 study demonstrated that their radiomics model for predicting postlaminar optic nerve tumor invasion, a significant risk factor for metastasis, surpassed radiologists' assessments in terms of sensitivity. Nevertheless, existing literature concerning the differentiation of retinoblastoma subtypes remains limited.

Consequently, the objective of this study was to distinguish $MYCN^{amp}RB1^{+/+}$ retinoblastoma from $RB1^{-/-}$ retinoblastoma utilizing quantitative radiomics on pretreatment MR imaging.

Methods

This retrospective multicenter case–control study was conducted in compliance with the STARD (Standards for Reporting Diagnostic accuracy studies) checklist and received approval from the institutional review board of the Amsterdam UMC. The necessity to obtain informed consent from participants was waived (IRB number IRB00002991).

Patients

This study utilized a patient cohort from a multicenter retrospective case–control study by Jansen et al.[21]. This patients were included from 10 tertiary retinoblastoma referral centers in 5 countries. In that study patients were included when 1) retinoblastoma was histopathologically confirmed; 2) unilateral disease; 3) availability of pretreatment MR images obtained after 1995 and at least included T1-weighted and T1-weighted contrast-enhanced MR images, and 4) availability genetic of analysis of tumor material. Cases of *MYCN*^{amp}*RB1*$^{+/+}$ retinoblastoma subtype were matched with controls (*RB1*$^{-/-}$ retinoblastoma with proven pathogenic variants in both alleles of the *RB1* gene) based on age, MRI scan date, and referral site at a ratio of 1:4. If controls could not be obtained in the same institution, controls from different institutions were used. The patient cohort consist of 110 retinoblastoma patients, including 22 *MYCN*^{amp}*RB1*$^{+/+}$ retinoblastoma cases and 88 *RB1*$^{-/-}$ retinoblastoma matched controls. In the current study, patients from the cohort were excluded if no T2-weighted MR images were available or if the images could not be processed or analyzed through the radiomics analysis pipeline (e.g. if tumor sizes were too small). If an *MYCN*^{amp}*RB1*$^{+/+}$ retinoblastoma case was excluded its controls were subsequently also deleted.

Quantitative MR imaging feature extraction and statistical methods for predicting *MYCN*-status

To enable quantitative feature extraction from MR images, the whole tumors were manually delineated on T2-weighted MR images using 3D Slicer (Version 4.10.1, MIT, USA). The delineation excluded non-enhancing areas of pure retinal detachment and subretinal fluid or hemorrhage. Expert radiologists (P.d.G. and M.d.J.) subsequently validated the manual delineations. All image processing and feature calculations were performed using the *PyRadiomics* package (version 3.1.0)[25]. MR images and delineations were resampled to 2x2x2 mm isotropic voxels and discretized using a fixed bin width of 64[25]. A total of 120 radiomics features were extracted from the delineated tumors, which could be divided into three main categories: intensity (n = 19), morphology (n = 26), and texture (n = 75). A previously used framework was employed to train a prediction models for *MYCN*-status and evaluate their performance using a cross-validation procedure[26].

This pipeline consists of a repeated cross-validation scheme that evaluates different combinations of feature selection methods, oversampling techniques, and classifiers to obtain an average classification performance for each configuration. Features were scaled using a z-score normalization. To reduce redundancy, features with a linear correlation above 0.8 with another feature were removed (removing the feature with the highest average correlation with the feature set). Four dimension reduction strategies were used: principal component analysis (PCA), recursive feature elimination in nested cross-validation using logistic regression (RFE-LR) and using random forests (RFE-RF), and a univariate selection method based the f-statistic from ANOVA (selecting the top 10 percentile). To address the inherently imbalanced dataset, oversampling of *MYCN*^{amp}*RB1*$^{+/+}$ retinoblastoma cases was applied using duplication of cases and interpolation (SMOTE). Two classifiers were evaluated: a logistic regression classifier (with L1 regularization) and a random forest classifier[27]. Model hyperparameters were optimized in nested cross-validation. For each combination of the aforementioned methods, a stratified repeated fivefold cross-validation approach was used to assess model generalizability. In every cross-validation fold, the model was trained on 80% of the samples and validated on the holdout subset of 20% of the samples. The fivefold cross-validation was repeated twenty times to further limit chance findings. Model performance was evaluated using the receiver-operator characteristic curve area-under-the-curve (AUC) was generated. The average AUC (with standard deviation [SD]) was calculated across the cross-validation iterations. The Brier score loss was calculated to additionally assess model calibration (0.0 being optimal[28]). For the best-performing combination of methods, the contribution of individual features to predictions were evaluated by calculating the SHAP values from a model trained on the whole dataset[29]. To assess whether the best-performing combination of methods exhibited significant performance beyond chance, random permutations were conducted. the repeated cross-validation procedure was repeated 1000 time using randomly shuffled labels, generating 1000 mean (cross-validated) AUCs representative of "random guessing". The resulting p value was defined as the fraction of repeated cross-validation iterations where the permutation mean AUC equaled or exceeded the observed mean AUC[30]. A schematic flowchart is shown in Fig. 1.

Results

Patients

Out of 110 patients in the cohort, 98 (89%) were included. Baseline characteristics of the patients are shown in Table 1 and examples of a case (*MYCN*^{amp}*RB1*$^{+/+}$ retinoblastoma) and a control (*RB1*$^{-/-}$ retinoblastoma) are shown in Fig. 2. A summary of MR imaging parameters can be found in Table S1. Twelve patients could not be evaluated: 1) one *MYCN*^{amp}*RB1*$^{+/+}$ patient had extensive extra-ocular disease outside of the analysis frame; 2) one *MYCN*^{amp}*RB1*$^{+/+}$ patient had no T2-weighted imaging; 3) eight matched control patients were subsequently excluded along with the abovementioned two *MYCN*^{amp}*RB1*$^{+/+}$ patients, and 4) two other control scans showed tumors with diameters below 5.38 mm and volume less than 63 mm^3 which were too small for *PyRadiomics* evaluation after resampling.

Classification performance

The best-performing combinations of methods was constructed by univariate feature selection, duplication of the *MYCN* features as means of oversampling, and logistic regression as classifier resulting in a mean AUC of 0.78 (SD 0.12; $p = 0.001$) with a mean Brier score of 0.20 (SD 0.05). The other combinations of methods had AUCs ranging 0.60 (SD 0.15) to 0.78 (SD 0.12). Performance of all radiomics models is shown in Table 2. For the best-performing combinations of methods, the SHAP values of the individual features are shown in Fig. 3. Of these three features, none were within the intensity category, two (66%) within the morphology category,

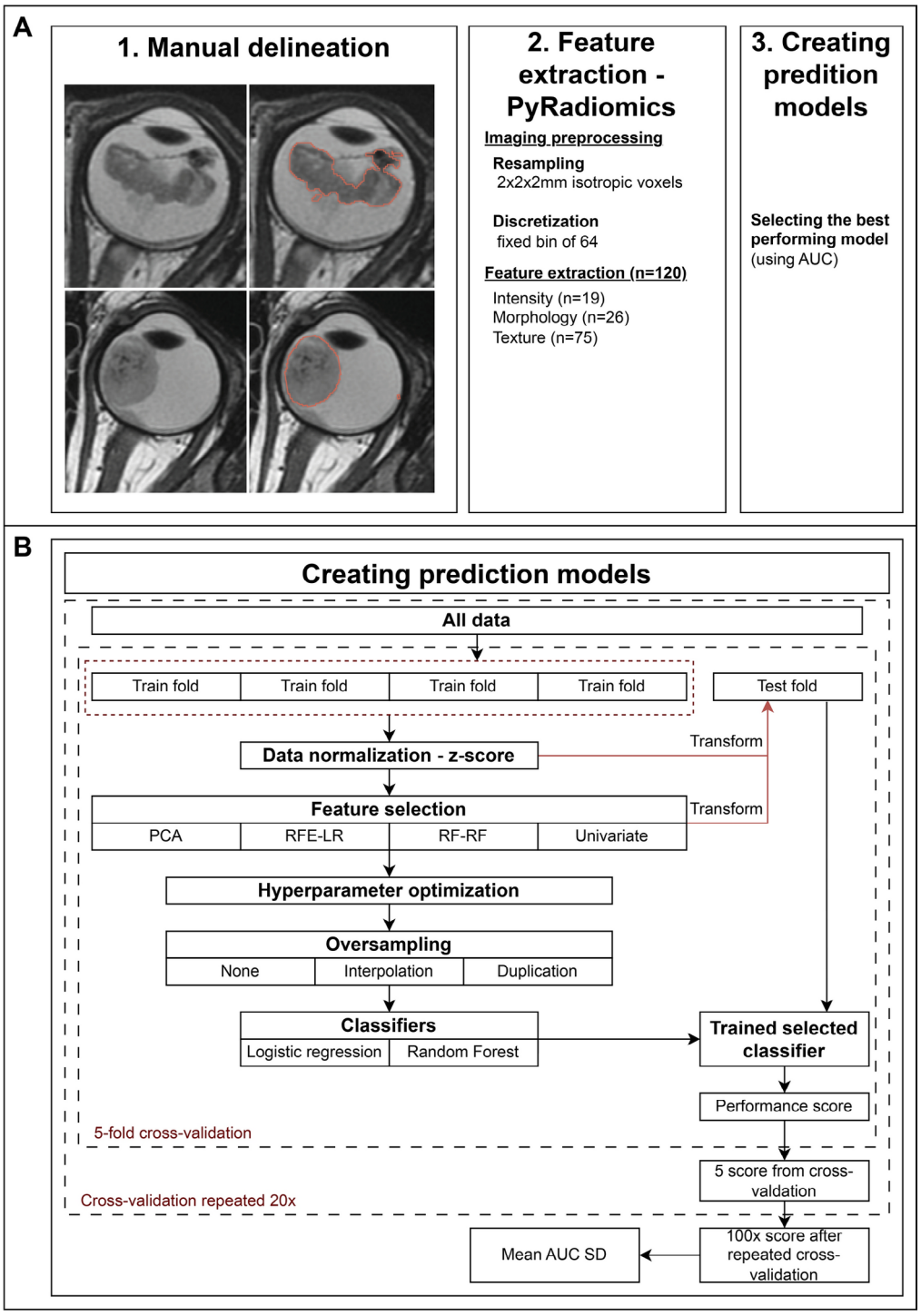

Fig. 1. Work flowchart of the study. (1) Manual delineation of the whole-tumor and validated by expert radiologists; (2) Processing data through *PyRadiomics* (version 3.1.0). (2.1) Resampling of MR imaging to 2×2×2 mm isotropic voxels and discretization by a 64 fixed bin. (2.2) Extracting 120 radiomics features divided into three categories: intensity (n = 19), morphology (n = 26), texture (n = 76); 3) Schematic framework of the creation of prediction models for *MYCN*-status utilizing different combinations of feature selection methods, oversampling techniques, and classifiers; (4) Selection and evaluation of the best-performing model. (4.1) Selection of the best-performing model by the highest mean AUC after the fivefold cross-validation which was 20 times repeated. (4.2) Evaluating the highest selected model by "random guessing" in which the original mean AUC was compared to permuted mean AUC. The permuted mean AUC was calculated by randomly shuffling the *MYCN* status and using it as input in the fivefold cross-validation which was repeated 20 times. This shuffling and 20 times repeated fivefold cross-validation was repeated 1000 times to obtain the permuted mean AUC.

	Total patients	Cases (*MYCN*^{amp}*RB1*$^{+/+}$ retinoblastoma)	Controls (*RB1*$^{-/-}$ retinoblastoma)	*p* value
Patients *n (%)*	98	20 (20%)	78 (80%)	
Female sex *n (%)*	44 (45%)	7 (35%)	37 (47%)	.440†
Laterality (left eye) *n (%)*	49 (50%)	9 (45%)	40 (51%)	.803†
Age in months at scan date; median, [IRQ], (range)	8 [5-12], (0-67)	7 [4-8], (3-42)	9 [5-13], (0-67)	.059§
MRI examination year, median [IRQ], (range)	2011 [2007–2015], (2001–2021)	2014 [2009–2017], (2002–2021)	2011 [2006–2015], (2001–2021)	.546§

Table 1. Patient demographics. *p* values were derived from † Fisher's exact test or § Mann Whitney U –test.

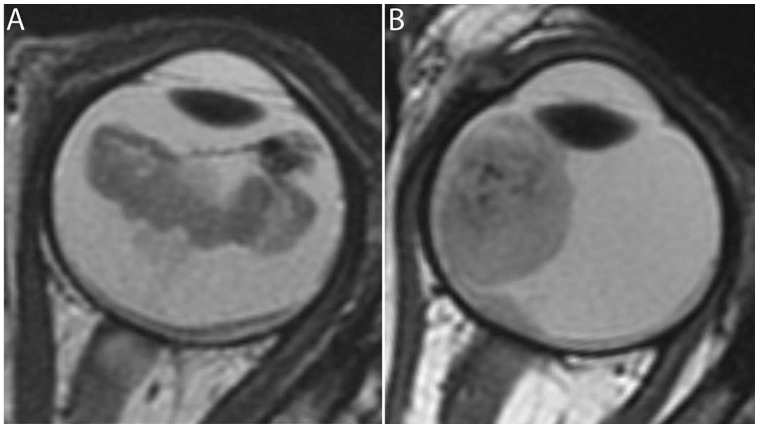

Fig. 2. MRI phenotype *MYCN*-amplified *RB1* wild-type (*MYCN*^{amp}*RB1*$^{+/+}$) retinoblastoma versus *RB1* pathogenic variation (*RB1*$^{-/-}$) retinoblastoma. (**A**) Axial 2D T2-weighted MR image of a 42-month-old patient with *MYCN*^{amp}*RB1*$^{+/+}$ retinoblastoma. The tumor has a diffuse growth pattern and is plaque shaped. Also, the intensity in the tumor varies greatly. (**B**) Axial 2D T2-weighted MR image of a 35-month-old patient with *RB1*$^{-/-}$ retinoblastoma. The tumor has an endophytic growth pattern and is dome shaped.

and one (33%) within the texture category. The morphology features were *sphericity* (morphologic resemblance to a sphere) and *flatness*, indicating that *MYCN*^{amp}*RB1*$^{+/+}$ tumors were less spherical and were flatter compared to *RB1*$^{-/-}$ retinoblastoma. The selected texture feature was *gray level non uniformity* indicating *MYCN*^{amp}*RB1*$^{+/+}$ tumors were more heterogeneous in terms of gray level distribution. Using these three features with logistic regression yielded a mean cross-validation AUC of 0.81 (SD 0.11).

Discussion

Due to their aggressive nature and relative resistance to typical chemotherapy approaches, identification of patients with *MYCN*-amplified *RB1* wild-type (*MYCN*^{amp}*RB1*$^{+/+}$) retinoblastoma might be clinically valuable in the future, although current treatment guidelines are not yet stratified according to genetic somatic alterations. As tissue biopsy is not considered safe in retinoblastoma, we sought to determine whether quantitative analysis of MR imaging could be used to identify this rare retinoblastoma subtype. However, there are promising results regarding aqueous humor liquid biopsy as a surrogate for tumor biopsy[31]. The various radiomics models based on the pretreatment T2-weighted MR images showed that *MYCN*^{amp}*RB1*$^{+/+}$ and *RB1*$^{-/-}$ retinoblastoma patients could be differentiated with an AUC of at least 0.60 up until 0.78. Eventually, the models could supplement the known clinical, ophthalmologic and qualitative MR imaging findings for pretreatment recognition of *MYCN*^{amp}*RB1*$^{+/+}$ retinoblastoma.

The use of radiomics analyses in research on retinoblastoma is scarce and only a limited number of published studies successfully used quantitative image analysis of retinoblastoma. A recent study investigating the ability of MR imaging-based radiomics features of the tumor to differentiate retinoblastoma with and without postlaminar optic nerve invasion resulted in a model with an AUC of 0.84[24]. In that study, a total of 2058 features were extracted and after feature selection only nine strongly correlated MRI features remained and were implemented in their prognostic model. Though individually appraising radiomics features is challenging, all of the features in our model could be linked to the tumor characteristics of *MYCN*^{amp}*RB1*$^{+/+}$ on MRI as reported by Jansen et al[21]. The two morphological features, *sphericity* and *flatness*, were respectively lower and higher in *MYCN*^{amp}*RB1*$^{+/+}$ tumors compared to *RB1*$^{-/-}$ controls, indicating that the *MYCN*^{amp}*RB1*$^{+/+}$ tumors were less spherical and more flat. This is consistent with the qualitative observations by Jansen et al. showing a more diffuse growth pattern in *MYCN*^{amp}*RB1*$^{+/+}$ tumors versus the bulkier mass lesions in *RB1*$^{-/-}$ tumors[21]. The texture feature in our model, *gray level non uniformity* was found to be higher in *MYCN*^{amp}*RB1*$^{+/+}$ retinoblastoma compared to *RB1*$^{-/-}$ controls. This suggests an increased variability in grey levels within *MYCN*^{amp}*RB1*$^{+/+}$ tumors as a sign of intratumoral heterogeneity, which could be related to the more aggressive nature of this subtype

Feature selection	Oversampling	Classifier	Mean AUC	AUC SD	Mean brier score	Brier score SD
Univariate	Duplicate	Logistic Regression	0.78	0.12	0.20	0.05
Univariate	Interpolate	Logistic Regression	0.78	0.12	0.20	0.05
Univariate	None	Logistic Regression	0.77	0.12	0.15	0.03
RFE-RF	None	Logistic Regression	0.76	0.12	0.15	0.03
RFE-RF	Duplicate	Logistic Regression	0.76	0.13	0.21	0.05
RFE-RF	Interpolate	Logistic Regression	0.75	0.13	0.21	0.05
RFE-LR	Duplicate	Logistic Regression	0.75	0.15	0.22	0.06
RFE-LR	None	Logistic Regression	0.74	0.15	0.16	0.05
RFE-LR	Interpolate	Logistic Regression	0.74	0.15	0.22	0.06
RFE-LR	None	Random Forest	0.66	0.13	0.16	0.03
RFE-LR	Duplicate	Random Forest	0.65	0.13	0.17	0.03
PCA	Duplicate	Logistic Regression	0.64	0.15	0.23	0.04
RFE-RF	None	Random Forest	0.64	0.13	0.16	0.03
PCA	Interpolate	Logistic Regression	0.64	0.15	0.23	0.05
PCA	Interpolate	Random Forest	0.64	0.15	0.18	0.04
PCA	Duplicate	Random Forest	0.64	0.15	0.17	0.03
RFE-RF	Duplicate	Random Forest	0.64	0.13	0.17	0.03
Univariate	Interpolate	Random Forest	0.64	0.14	0.21	0.05
RFE-LR	Interpolate	Random Forest	0.63	0.14	0.18	0.03
RFE-RF	Interpolate	Random Forest	0.63	0.13	0.18	0.03
PCA	None	Logistic Regression	0.63	0.15	0.19	0.04
PCA	None	Random Forest	0.63	0.16	0.16	0.03
Univariate	None	Random Forest	0.62	0.15	0.17	0.04
Univariate	Duplicate	Random Forest	0.60	0.15	0.19	0.05

Table 2. Radiomics models predicting *MYCN*-status. Results from all cross-validation analyses (PCA: principal component analysis; RFE-RF: a recursive feature elimination approach using a random forest in nested cross-validation; Univariate: a univariate selection method based on ANOVA testing that retained the top 10 percentile features; AUC: area under the curve; SD: standard deviation; Brier score assesses the model calibration and refinement [0.0 being optimal]).

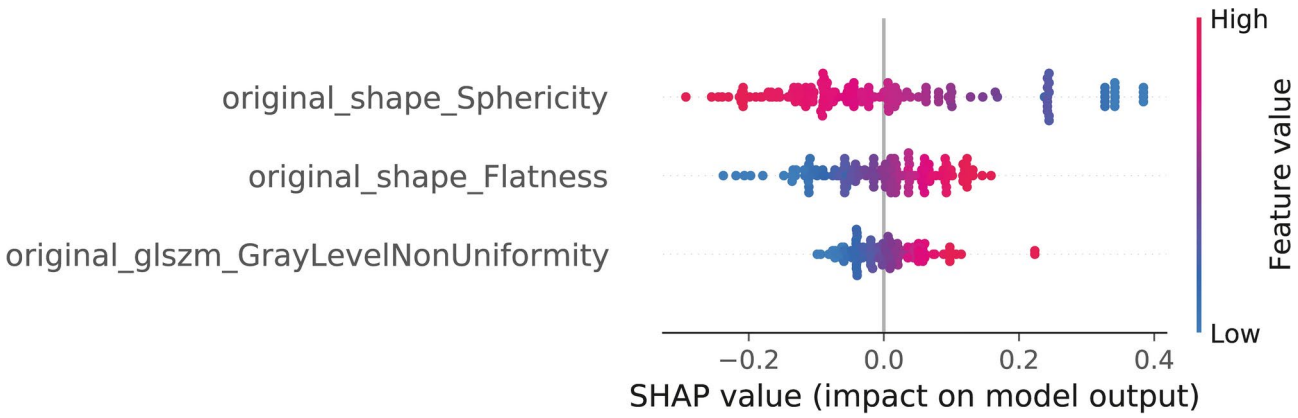

Fig. 3. All features in the best-performing model with univariate feature selecting, duplicate scaling, and a logistic regression as classifier. Features in three categories were assessed: Intensity features, texture features and morphology features. Intensity features comprised of first order statistics [19 features]. Morphology features comprised of shaped-based 2D features [10 features] and 3D features [16 features]. Texture features comprised on features based on gray-level co-occurrence matrices (GLCM) [24 features], gray-level run length matrices (GLRLM) [16 features], gray-level size zone matrices (GLSZM) [16 features], neighborhood gray-tone difference matrices (NGTDM) [5 features], and gray-level dependence matrices (GLDM) [14 features]. Original_shape_Sphericity = *original shape sphericity*; original_shape_Flatness = *original shape flatness*; original_glszm_GrayLevelNonUniformity = *Original glszm gray level non uniformity*.

of retinoblastoma. Notably, this is in line with two recently identified features of peritumoral hemorrhage and subretinal hemorrhage associated with the fast-growing *MYCN*^{amp}*RB1*$^{+/+}$ tumors[21]. This correlation between qualitative features and quantitative features strengthens the suggestion that radiomics models may well become powerful supportive tools for subtype recognition in retinoblastoma, especially when predictive models combine clinical characteristics and ophthalmological and qualitative radiological features.

There were several limitations of this study. The subtype *MYCN*^{amp}*RB1*$^{+/+}$ is rare and cases with MR imaging available world-wide are limited and MR imaging acquisition protocols and quality varied within and between centers. Another consequence of the rarity of this tumor subtype was the unavailability of a separate validation cohort for the current study. To address this, a fivefold cross-validation was used to assess model generalization. Also, the case–control design of the study might have inflated the accuracy results, as there was an overrepresentation of *MYCN*cases in the study setting compared to clinical practice[32]. Last, some of the strong clinical predictors of *MYCN*^{amp}*RB1*$^{+/+}$ such as a young-age at presentation and unilaterality could not be incorporated in our analyses due to the case–control study design[9]. Combination of these strong clinical predictors with the quantitative features obtained through radiomics might result in an even an better prediction of higher AUC for predicting *MYCN* status.

In conclusion, this study demonstrated the feasibility of distinguishing between *MYCN*^{amp}*RB1*$^{+/+}$ and *RB1*$^{-/-}$ tumors using quantitative imaging analysis. Facilitating early detection of this more aggressive retinoblastoma subtype, *MYCN*^{amp}*RB1*$^{+/+}$, and may aid in selecting personalized treatments, ultimately improving future outcomes.

Data Availability

The data that support the findings of this study are not openly available due to reasons of sensitivity and are available from the corresponding author upon reasonable request, only if permission of the providing center is obtained.

Received: 16 May 2024; Accepted: 17 October 2024
Published online: 23 October 2024

References

1. Moll, A. C. et al. Incidence and survival of retinoblastoma in The Netherlands: a register based study 1862–1995. *Br J Ophthalmol* **81**(7), 559–562 (1997).
2. Pritchard, E. M., Dyer, M. A. & Guy, R. K. Progress in Small Molecule Therapeutics for the Treatment of Retinoblastoma. *Mini Rev Med Chem* **16**(6), 430–454 (2016).
3. Aubry, A., Yu, T. & Bremner, R. Preclinical studies reveal MLN4924 is a promising new retinoblastoma therapy. *Cell Death Discov* **6**, 2 (2020).
4. Kooi, I. E. et al. Loss of photoreceptorness and gain of genomic alterations in retinoblastoma reveal tumor progression. *Ebiomedicine* **2**(7), 660–670 (2015).
5. Afshar, A. R. et al. Next-Generation Sequencing of Retinoblastoma Identifies Pathogenic Alterations beyond RB1 Inactivation That Correlate with Aggressive Histopathologic Features. *Ophthalmology* **127**(6), 804–813 (2020).
6. Schaiquevich, P. et al. Treatment of Retinoblastoma: What Is the Latest and What Is the Future. *Front. Oncol.* **12**, 822330 (2022).
7. Kapatai, G. et al. Gene expression profiling identifies different sub-types of retinoblastoma. *Br J Cancer* **109**(2), 512–525 (2013).
8. Liu, J. et al. A high-risk retinoblastoma subtype with stemness features, dedifferentiated cone states and neuronal/ganglion cell gene expression. *Nat Commun* **12**(1), 5578 (2021).
9. Rushlow, D. E. et al. Characterisation of retinoblastomas without RB1 mutations: genomic, gene expression, and clinical studies. *Lancet Oncol* **14**(4), 327–334 (2013).
10. Ewens, K. G. et al. Phosphorylation of pRb: mechanism for RB pathway inactivation in MYCN-amplified retinoblastoma. *Cancer Med* **6**(3), 619–630 (2017).
11. Singh, H. P. et al. An immature, dedifferentiated, and lineage-deconstrained cone precursor origin of N-Myc-initiated retinoblastoma. *Proc Natl Acad Sci U S A* **119**(28), e2200721119 (2022).
12. Price, E. A. et al. MYCN amplification levels in primary retinoblastoma tumors analyzed by Multiple Ligation-dependent Probe Amplification. *Ophthalmic Genet* **42**(5), 604–611 (2021).
13. Lillington, D. M. et al. High level amplification of N-MYC is not associated with adverse histology or outcome in primary retinoblastoma tumours. *Br J Cancer* **87**(7), 779–782 (2002).
14. Zugbi, S., et al., *Clinical, Genomic, and Pharmacological Study of MYCN-Amplified RB1 Wild-Type Metastatic Retinoblastoma.* Cancers, 2020. **12**(9).
15. Abramson, D. H., Gobin, Y. P. & Francis, J. H. Orbital Retinoblastoma Treated with Intra-arterial Chemotherapy. *Ophthalmology* **128**(10), 1437 (2021).
16. Zhou, C., et al., *Eye-Preserving Therapies for Advanced Retinoblastoma: A Multicenter Cohort of 1678 Patients in China.* Ophthalmology, 2021.
17. Berry, J. L. et al. Genomic cfDNA Analysis of Aqueous Humor in Retinoblastoma Predicts Eye Salvage: The Surrogate Tumor Biopsy for Retinoblastoma. *Molecular cancer research : MCR* **16**(11), 1701–1712 (2018).
18. De Jong, M. C. et al. Diagnostic Accuracy of Intraocular Tumor Size Measured with MR Imaging in the Prediction of Postlaminar Optic Nerve Invasion and Massive Choroidal Invasion of Retinoblastoma. *Radiology* **279**(3), 817–826 (2016).
19. de Graaf, P. et al. Guidelines for imaging retinoblastoma: imaging principles and MRI standardization. *Pediatr Radiol* **42**(1), 2–14 (2012).
20. de Jong, M. C. et al. Trilateral retinoblastoma: a systematic review and meta-analysis. *Lancet Oncol* **15**(10), 1157–1167 (2014).
21. Jansen, R. W. et al. MRI Features for Identifying MYCN-amplified RB1 Wild-type Retinoblastoma. *Radiology* **307**(5), e222264 (2023).
22. Lambin, P. et al. Radiomics: the bridge between medical imaging and personalized medicine. *Nature reviews Clinical oncology* **14**(12), 749–762 (2017).
23. Strijbis, V. I. J. et al. Multi-view convolutional neural networks for automated ocular structure and tumor segmentation in retinoblastoma. *Sci Rep* **11**(1), 14590 (2021).
24. Li, Z., et al., *MRI-based radiomics model can improve the predictive performance of postlaminar optic nerve invasion in retinoblastoma.* The British Journal of Radiology, 2022. **95**(1130).
25. van Griethuysen, J. J. M. et al. Computational Radiomics System to Decode the Radiographic Phenotype. *Cancer Res* **77**(21), e104–e107 (2017).

26. Cysouw, M. C. F. et al. Machine learning-based analysis of [(18)F]DCFPyL PET radiomics for risk stratification in primary prostate cancer. *Eur J Nucl Med Mol Imaging* **48**(2), 340–349 (2021).
27. Breiman, L. Random Forests. *Machine Learning* **45**, 5–32 (2001).
28. Murphy, A.H., *A New Vector Partition of the Probability Score.* Journal of Applied Meteorology and Climatology, 1973. **12**(4).
29. Lundberg, S.M. and S.-I. Lee, *A unified approach to interpreting model predictions.* Advances in neural information processing systems, 2017. **30**.
30. Ojala, M. and G.C. Garriga, *Permutation tests for studying classifier performance.* Journal of machine learning research, 2010. **11**(6).
31. Xu, L., et al., *Establishing the Clinical Utility of ctDNA Analysis for Diagnosis, Prognosis, and Treatment Monitoring of Retinoblastoma: The Aqueous Humor Liquid Biopsy.* Cancers (Basel), 2021. **13**(6).
32. Yuan, W. et al. Temporal bias in case-control design: preventing reliable predictions of the future. *Nat Commun* **12**(1), 1107 (2021).

Author contributions

Guarantors of integrity of entire study, C.M.d.B., R.W.J., P.M., P.d.G. ; study concepts/study design or data acquisition or data analysis/interpretation, all authors; manuscript drafting or manuscript revision for important intellectual content, all authors; approval of final version of submitted manuscript, all authors; agrees to ensure any questions related to the work are appropriately resolved, all authors; literature research, C.M.d.B., R.W.J., A.H.S., P.M., S. Sirin., J.D. ; clinical studies, C.M.d.B., J.L.J., A.H.S., A.K.M., P.M., O.E.U., H.G., R.C.B., S. Sen, M.K., S. Sirin, H.J.B., P.G., C.J.D., M.C., A.C.M., P.d.G. ; experimental studies, C.M.d.B., R.W.J., S.v.E., S. Sen, M.C., R.B., J.D. ; statistical analysis, C.M.d.B., R.W.J., M.C., M.C.d.J. ; and manuscript editing, C.M.d.B., R.W.J., L.C., S.G., S.v.E., J.L.J., A.R., A.H.S., A.K.M., P.M., O.E.U., G.B.H., H.G., H.C.B., K.E.N., R.C.B., S. Sen, M.K. S. Sirin, H.J.B., P.G., C.J.D., M.C., R.B., J.D., A.C.M., M.C.d.J., P.d.G.

Funding

Initiation and coordination of this study was funded by Stichting Kinderen Kankervrij (KIKA) (grant no. 342) and the Hanarth Foundation (grant for project titled MRI-based Deep Learning Segmentation and Quantitative Radiomics in Retinoblastoma: A Next Step Toward Personalized Interventions). Departmental funding was received by Casey Eye Institute, Oregon Health & Science University (A.H.S., A.K.M., and O.E.U.) from the National Institutes of Health (grant P30 EY010572) in addition to unrestricted departmental funding from Research to Prevent Blindness. Departmental funding was received by Emory Eye Center, Ocular Oncology Service (O.E.U., G.B.H., and H.G.) via National Eye Institute core grant P30 EY006360.

Declarations

Conflict of interests

C.M.d.B. No relevant relationships. R.W.J. No relevant relationships. L.C. No relevant relationships. S.G. No relevant relationships. S.v.E. No relevant relationships. J.L.J. No relevant relationships. A.R. No relevant relationships. A.H.S. No relevant relationships. A.K.M. No relevant relationships. P.M. No relevant relationships. O.E.U. No relevant relationships. G.B.H. No relevant relationships. H.G. No relevant relationships. H.C.B. No relevant relationships. K.E.N. No relevant relationships. R.C.B. Consultant for Aileron Therapeutics. S. Sen No relevant relationships. M.K. No relevant relationships. S. Sirin No relevant relationships. H.J.B. No relevant relationships. P.G. No relevant relationships. C.J.D. No relevant relationships. M.C. No relevant relationships. R.B. No relevant relationships. J.D. No relevant relationships. A.C.M. No relevant relationships. M.C.d.J. No relevant relationships. P.d.G. No relevant relationships.

Additional information

Supplementary Information The online version contains supplementary material available at https://doi.org/10.1038/s41598-024-76933-6.

Correspondence and requests for materials should be addressed to C.M.B.